ACS OMEGA

Open Access

http://pubs.acs.org/journal/acsodf

Article

Surface Reconstruction and Layer-Dependent Semiconductor-to-Metal Transition of Zinc-Blende CdSe

Yuexin Dong, Kaiyun Chen,* Songrui Wei, Le Zhang, Haoxi Dong, Cunle Bo, and Wangtu Huo*

Cite This: *ACS Omega* 2024, 9, 42488−42497

Read Online

ACCESS | Metrics & More | Article Recommendations | Supporting Information

ABSTRACT: In this work, CdSe was taken as the representation to systematically investigate the (111) and (110) surface reconstructions, the electronic properties transition related to the layer size, and the corresponding physical mechanism through the density functional theory (DFT) calculation. For the (111) surface slab structure, the bulk truncated relaxation (BTR) surface and the honeycomb (HC) surface were carefully examined. The HC surface configuration, ignored by previous studies, is an energetically preferred surface compared to both the as-truncated and BTR configurations. Based on the HC surface, the band structure of the (111) surface shows a semiconductor character below four layers (4L). Surprisingly, the (111) CdSe turns metallic in the 4L system. In a higher-layer (>4L) system, the two side surfaces and internal regions show metallic and semiconductivity features, respectively. Such an abundant electronic properties transition should be attributed to the electron transfer under the intrinsic polarization perpendicular to the asymmetrical (111) plane. Different from the (111) surface, drastic structural reconstructions were not observed in the (110) surface and the band gap gradually decreased with the increasing number of layers until it approached the value in the bulk. Our results not only revealed the additional possible surface structure but also clarified the underlying mechanism of semiconductor-to-metal (even the edge metallic) transition related to the number of layers. All these findings could be extended to other II−VI group MX compounds for further development of electronic devices.

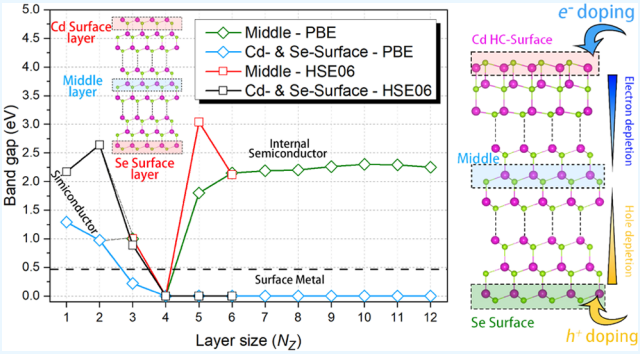

INTRODUCTION

Photovoltaic materials play a role in converting light energy to electrical energy and are widely used in photodetectors, solar cells, fiber optic communications, and photoelectric sensors.[1−4] Due to their special structural character, low-dimensional photovoltaic materials can generate diverse novel physical properties enabling great advancement in photonic devices with improved efficiency, speed, transparency, wavelength range, flexibility, integrability, etc.[5,6] All of the above excellent potential photovoltaic performance promotes more attention to preparing low-dimensional materials including the quantum dot (0D), nanoribbon (1D), film (2D), etc.[7−11]

The low-dimensional van der Waals (vdW) materials were first exfoliated in experiments due to the naturally weak interlayer vdW interaction.[12−15] Some of them, such as silicene, phosphorene, and transition-metal dichalcogenides, show a direct band gap ranging from 0.3 to 2.10 eV.[16−19] They suggest the potential broad applications in ultrasensitive light detection devices ranging from ultraviolet (UV) to far-infrared (FIR) ranges.[20−23] In addition to vdW materials, the exfoliation of the covalent materials also attracts great interest. Owing to the stronger covalent bond, the dangling bond will induce various unique properties once the surface state is cleaved from the bulk structure including surface (edge) reconstruction, semiconductor−metallic transition, magnetism, high-efficiency catalysis, etc.[24−27] Therefore, the edge structure and the layer number of nanomaterials significantly determine their properties. For example, the armchair and zigzag nanoribbons of $PtSe_2$ show metallic and semiconductor properties, respectively.[28] Furthermore, many other properties (magnetism, band structures, spin polarization, and elastic properties) also depend on the layer number of nanostructures, e.g., the width of nanoribbons and the diameter of nanoparticles.[29]

Recently, cadmium chalcogenides (CdX, X = S, Se, and Te), as a typical photovoltaic material of the II−IV group, have attracted much more attention because of the combination of excellent electronic properties, optical properties, and high quantum yields.[30,31] In addition, many theoretical and experimental advances suggested that the electronic and

Received: July 12, 2024
Revised: September 19, 2024
Accepted: September 23, 2024
Published: October 4, 2024

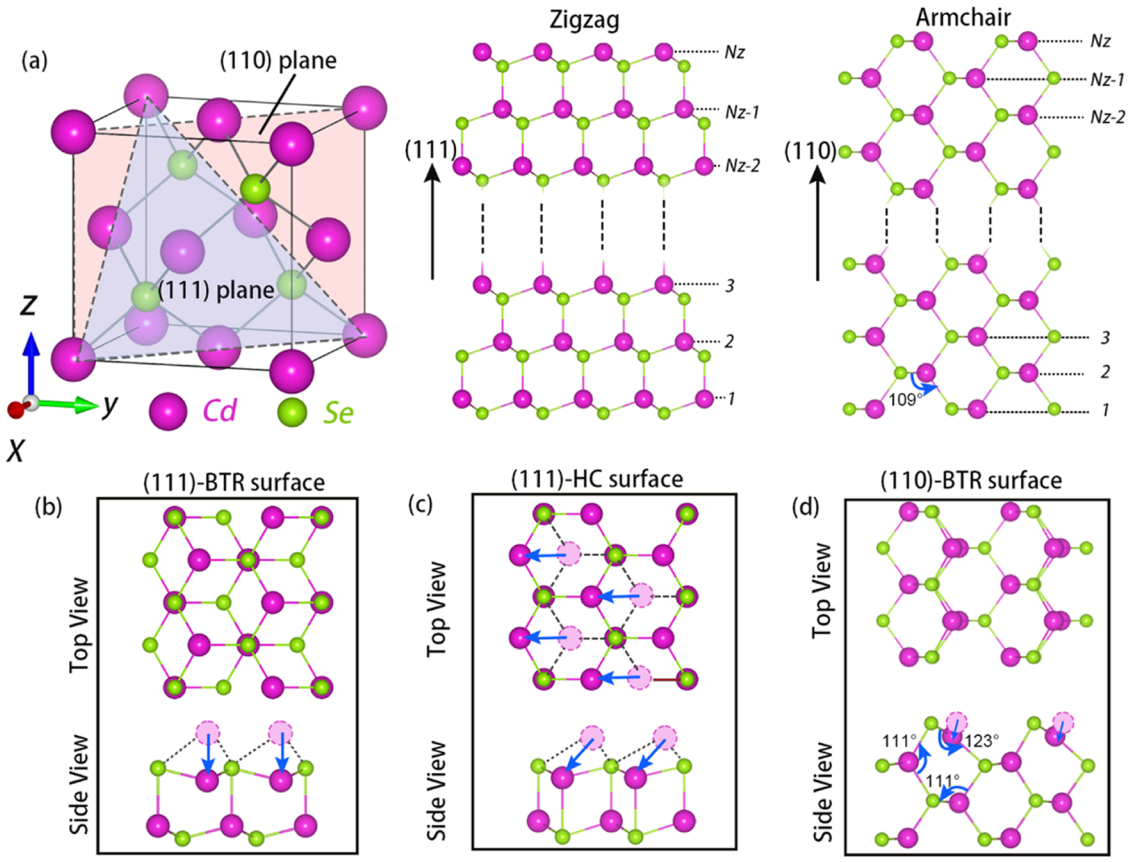

Figure 1. Crystal structure of CdSe. (a) Crystal structure of bulk. The (111) and (110) planes are denoted by gray and pink planes, respectively. (b) Cd-terminated surface reconstruction after truncation from the (111) plane and fully relaxed (BTR). (c) Honeycomb (HC) reconstruction of the Cd-terminated (111) surface. (d) (110) Surface reconstruction. Blue arrows in (b−d) indicate the displacements of surface Cd atoms.

optical properties of CdX can be efficiently modulated by manipulating the physical dimensions.[32,33] For example, quantum confinement effects (QCEs) are observed in dimension-reduced nanomaterials of CdX including colloidal 0D quantum dots (QDs)[34,35] and 1D nanoribbons (wires, rods, and belts).[36−38] Recently, Devi et al. also reported layer-number-dependent stability and electronic properties of CdX (X = S, Se, and Te) based on the (0001) surface slabs of wurtzite (WZ) CdX compounds.[39] The unique band gap oscillations accompanied by the layer variation are observed in CdSe and CdTe, i.e., metallic and semiconductor for even- and odd-layer systems, respectively.

In addition to the WZ phase, CdX also shows another zinc blende (ZB) phase with stability similar to that of the WZ phase. Based on the different stacking order compared to WZ,[40] ZB CdX should present many other possible properties. The as-truncated (111) and (110) surfaces are characterized by zigzags and armchairs, respectively. There is an intrinsic polarization in the asymmetric (111) surface, and there is no polarization in the symmetric (110) surface. Such characteristics of these two surfaces have attracted much attention in previous studies and show great interesting properties.[41,42] However, many previous theoretical studies always focus on the monolayer (1L) or bilayer (2L) ZB CdX.[43,44] As reported by Zhou et al., the ZB (111) CdX seems to present surface reconstruction when layers are limited below 3.[44] Confusingly, surface reconstruction disappears as the layers increase beyond 4. The surface structure seems to be contradictory to the 2L honeycomb structure found by Lucking et al. in 2L III−V, II−VI, and I−VII zinc-blende semiconductors.[45] Therefore, some additional surface reconstructions were ignored by previous studies despite the extensive work that has already been reported about CdSe. Furthermore, the (111) CdSe shows the layer-size-dependent transition of electronic structures. The mono- and bilayer systems are direct semiconductors. In addition, the 3L ZB (111) CdX is still classified as a direct semiconductor despite both the conduction band bottom (CBM) and valence band bottom (VBM) crossing the Fermi level already. Furthermore, the band gap of 3L ZB (111) CdX is only ∼0.04 eV with a HSE06 hybrid functional correction.[44] It is expected that the surface reconstruction may induce layer-dependent properties of ZB (111) CdX, such as metallic transition. Therefore, there are still existing misunderstandings about ZB CdX referring to surface reconstruction, layer-number-dependent electronic structure, and the underlying mechanisms of a possible metallic transition with increasing layers. In this work, the density functional theory (DFT) calculations were adopted to investigate the (111) and (110) surface reconstructions and the electronic structures of CdSe from 1L to 12L. We found that the honeycomb surface configuration is energetically preferred, which is ignored by previous studies. Furthermore, the (111) slab is much more sensitive to the layer number compared to the (110) slab. The (111) CdSe shows the semiconductor (1L, 2L, and 3L), metallic (4L), and surface metallic state (>4L), i.e., metallic and semiconductor state at the surface and in the internal region, as layers increase. On the contrary, the band structures

https://doi.org/10.1021/acsomega.4c06465
ACS Omega 2024, 9, 42488−42497

of the reconstructed (110) surface slabs always show semiconductivity and are independent of layer number.

RESULTS AND DISCUSSION

Crystal Structure and Surface Reconstruction of ZB CdSe. Figure 1a depicts the bulk crystal structure of ZB CdSe with the $F\bar{4}3m$ space group, which is very similar to that of SiC.[46,47] The unit cell of CdSe is cubic, featuring eight Cd atoms positioned at each of the eight corners, six Cd atoms at the center of each face, and four Se atoms within the cube. After complete relaxation, the lattice constant of the bulk CdSe is $a = b = c = 6.21$ Å, while all three angles are 90°, i.e., $\alpha = \beta = \gamma = 90°$. The bond length of Cd−Se is 2.69 Å. In addition to the crystal structure, the corresponding band structure was calculated and is shown in Figure S1. The bulk CdSe shows the direct semiconductor with a ∼0.48 eV gap by using the PBE functional. All these results agreed well with both previous theoretical and experimental results, ensuring the reasonability of parameters in our calculation.[48,49]

As shown in Figure 1a, the blue triangle and pink rectangle denote the (111) and (110) planes, respectively. Accordingly, the bulk CdSe were truncated to two surface structures from the (111) and (110) planes and are shown in the right region of Figure 1. Here, the (111) and (110) surfaces were arranged perpendicular to the z-direction in these two truncated slab structures. The thickness of these two slabs (N_Z) is defined as the number of Cd layers along the z-direction. In order to keep the stoichiometric ratio in the asymmetrical (111) surface structure, the atoms at the bottom and top surfaces are those of Se and Cd, respectively. Clearly, the as-truncated (111) and (110) surfaces present zigzag and armchair characters, respectively. Here, we also calculated the surface formation energies of the (111), (110), and (100) surfaces (see Table S2). Both (111) and (110) are significantly more stable than the (100) surface due to the positive value of (100). The as-truncated structures with N_Z changing from 1L to 12L were fully relaxed and are presented in Figures S2 and S3. Some new surface configurations at the Cd-terminated surface can be observed (highlighted by red dash boxes). For more convenience, the top and side views of the (111) slab with the spontaneous surface reconstruction are schematically shown in Figure 1b. The pink dotted circle stands for the initial position of Cd in the as-truncated structure. Obviously, the Cd atoms at the Cd-terminated surface show significant spontaneous inward displacement toward the neighboring Cd after complete relaxation but without the in-plane movement. This surface structure is energetically favorable, e.g., energy reduction is ∼0.25 eV in the $N_Z = 6$ slab. The Cd atoms shift inward, leading to the Cd−Cd interatomic distance at the Cd surface reducing from ∼4.39 to ∼3.45 Å. At the Se-terminated surface, despite the Cd−Se bond length reducing from ∼2.69 to ∼2.97 Å, there is no obvious reconstruction of surface structures after full relaxation. Such reconstructed surface structure is named as bulk truncated relaxation (BTR) surface, which is also observed in the bilayer III−V, II−VI, and I−VII 2D materials such as InSb, InAs, GaSb, GaAs, and HgTe.[45]

In addition, there is also another possible surface reconstruction with both out-of-plane and in-plane Cd displacement in the (111) surface, as depicted in Figure 1c, i.e., Cd moves to the top of Se at the adjacent inside layer. After that, the (111) surface structure shows the honeycomb (HC) character. This surface configuration was reported in 2L II−VI group compounds by Lucking.[45] Furthermore, a ∼0.61 eV energy barrier can be observed from BTR to HC in 3L (111) ZB CdSe, as shown in Figure S4. Such a large barrier will prevent the spontaneous transition from BTR to HC despite the HC configuration being more stable than BTR. Here, we also calculate the energy of the HC surface in the $N_Z = 2$ and 6 (111) surface structures. The energy reductions are ∼0.88 eV ($N_Z = 2$) and ∼0.33 eV ($N_Z = 6$) compared to the as-truncated surface. In other words, the HC surface should be the most stable configuration in the (111) surface structure.

Figure S3 summarizes the crystal structures of the (110) surface structure from $N_Z = 1$ to 12 after full relaxation. The as-truncated Cd-terminated surface is still unstable and spontaneously moves inside. Figure 1d depicts the (110) surface structure after full relaxation. Despite the (110) surface having no notable structural change after relaxation compared to the (111) slabs, the surface Cd still shows inward displacement to the inside layer forming the Cd−Se plane. Here, we also measure the Se−Cd−Se bond angle. It increases from ∼109 to 123°. In addition, the ∼0.98 eV energy decrease compared to the as-truncated surface could be obtained in $N_Z = 2$ (110) surface structure. Here, we also manually construct the different surface configurations of Cd atoms, including moving Cd to the internal position and in-plane displacement. All of these structures still spontaneously return back to the (110)-BTR surface, as depicted in Figure 1d.

Mechanism of Surface Reconstruction. According to the crystal structure of the (111) surface structure in Figure S2, the Cd−Se bonds are broken when the bulk CdSe is truncated, i.e., the surface cutting breaks the Cd−Se bonds at the Cd-terminated surface. Considering the as-truncated structure along the (111) plane should be a polarized structure (Figure 1a) such as (111)-SiC,[50,51] the polarization discontinuity in the as-truncated structure generates a negative charge at the Se-terminated surface and a positive charge at the Cd-terminated surface. It will drive certain electron transfer from the Se-terminated surface to the Cd-terminated surface. This is confirmed by the Bader analysis summarized in Table 1. For example, the negative charge of Se1 at the Se-terminated surface decreases from $6.72e^-$ in bulk CdSe to $6.58e^-$ in the as-truncated structure. Meanwhile, the negative charge of Cd at the Cd-terminated surface increases from $11.29e^-$ in bulk CdSe to $11.43e^-$ in the as-truncated structure. Therefore, $\sim 0.14e^-$ from the Se surface to the Cd surface can be observed in the $N_Z = 6$ system. Consequently, these unpaired electrons forming the dangling bonds on Cd greatly increase the instability of the Cd-terminated surface.

Table 1. Negative Charge of Cd and Se at the (111) and (110) Surfaces in As-Truncated, BTR, and HC $N_Z = 6$ Surface Structures[a]

		(111) as-truncated	(111) BTR	(111) HC	(110) as-truncated	(110) BTR
Cd surface	Cd	11.43	11.35	11.36	11.28	11.30
	Se1	6.67	6.69	6.67	6.74	16.67
	Se2	6.70	6.69	6.74	6.72	6.73
Se surface	Cd	11.28	11.29	11.28	11.28	11.31
	Se1	6.58	6.62	6.60	6.74	6.67
	Se2	6.71	6.72	6.73	6.71	6.73

[a]The notion of each atom corresponds to that in Figure 2. The electron number in the POTCAR file is 12 and 6 for Cd and Se single atoms.

https://doi.org/10.1021/acsomega.4c06465
ACS Omega 2024, 9, 42488−42497

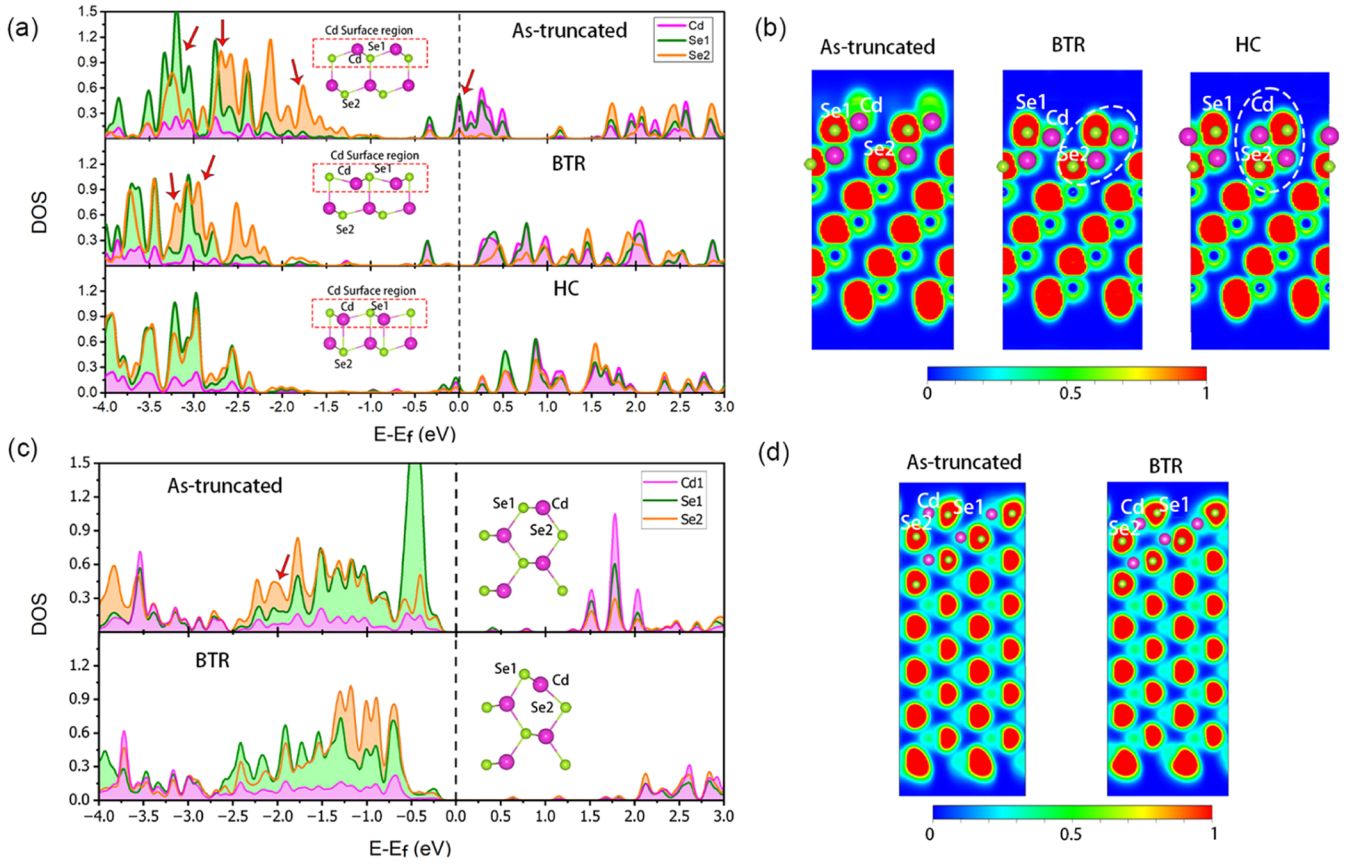

Figure 2. Electron projection density of states (PDOS) of Cd and Se atoms of the $N_Z = 6$ surface structure. (a) PDOS of Cd and neighboring Se at the bare Cd surface in the (111) as-truncated, BTR, and HC surfaces. (b) ELF of the as-truncated, BTR, and HC surfaces in the (111) slab model. (c) PDOS of Cd and neighboring Se at the bare Cd surface in the (110) as-truncated and BTR surfaces. (d) ELF of the as-truncated and BTR surfaces in the (110) slab model. The positions of the Cd, Se1, and Se2 atoms are labeled in the diagram.

To reduce the total energy of the whole system, the (111) slab should undergo spontaneous structure reconstruction to self-passivate the unpaired electrons at the surface of Cd. As shown in Figure 2a, the PDOS peak of the BTR surface shifts to a lower energy level compared with the as-truncated structure, especially the peak at the (−2.0, −1.0) eV range from the Fermi level, suggesting that the BTR structure is energetically favorable. Such a result is consistent with the results in Table S1. Furthermore, the electron density on the surface of Cd obviously decreases, as shown in the corresponding ELF in Figure 2b. Despite slight negative charge changes in the BTR surface as listed in Table 1, i.e., electrons slightly decrease on the surface Cd atoms, unpaired electrons (dangling bonds) of surface Cd are redistributed and passivated according to the energetically favorable PDOS and ELF. The bare Cd surface, therefore, undergoes observable inward displacement of Cd and spontaneous structural reconstruction from the as-truncated structure to BTR, which is similar to the edge reconstruction in other low-dimensional structures including TMDs and black phosphorus.[52,53]

However, the PDOS values between Cd and Se2 did not completely match with each other in the BTR surface. This should be the reason that BTR has a metastable structure, according to previous results. Here, we also present the PDOS of the HC (111) surface structure of $N_Z = 6$ in Figure 2a. When the Cd surface turns to the HC configuration, the PDOS peak of each atom further shifts to a lower energy level compared with both the as-truncated and BTR surfaces. Another obvious characteristic is that the PDOS of Cd and all Se (Se1 and Se2) show very similar peaks at the same energy level. The corresponding ELF in Figure 2b shows significantly weak electron density at the top of surface Cd but more in the top two interlayer regions between Cd and Se2, indicating the enhanced interlayer interaction at the top two layers highlighted by a white dot circle. Such results suggest that the reconstructed HC surface configuration can eliminate more dangling bonds on Cd and enhance the bonding between Cd and Se2, increasing the stability of HC configuration compared to BTR. That is why the HC configuration is the most stable and energetically favorable.

For the (110) surface structure, the Cd−Se bonds in the bulk are also broken along the (110) plane after the surface formation. Different from the (111) plane, there is no intrinsic polarization between the two surfaces because the as-truncated (110) surface structure is symmetrical on both sides. Bader analysis in Table 1 confirms this to be due to the very close negative charge at the two side surfaces of $N_Z = 6$. In other words, the additional electrons cannot be transferred from one surface to another. Figure 2c presents the PDOS (Cd and two neighboring Se) of the (110) as-truncated and BTR structures, respectively. For the as-truncated surface structure, the intensity peaks of Cd and Se1 are quite different at the (−0.75, −0.25) eV range, where Se1 shows a very large intensity compared to Cd. In addition, Cd and Se2 also show mismatch peaks around −2.1 eV, denoted by red arrows. All

https://doi.org/10.1021/acsomega.4c06465
ACS Omega 2024, 9, 42488−42497

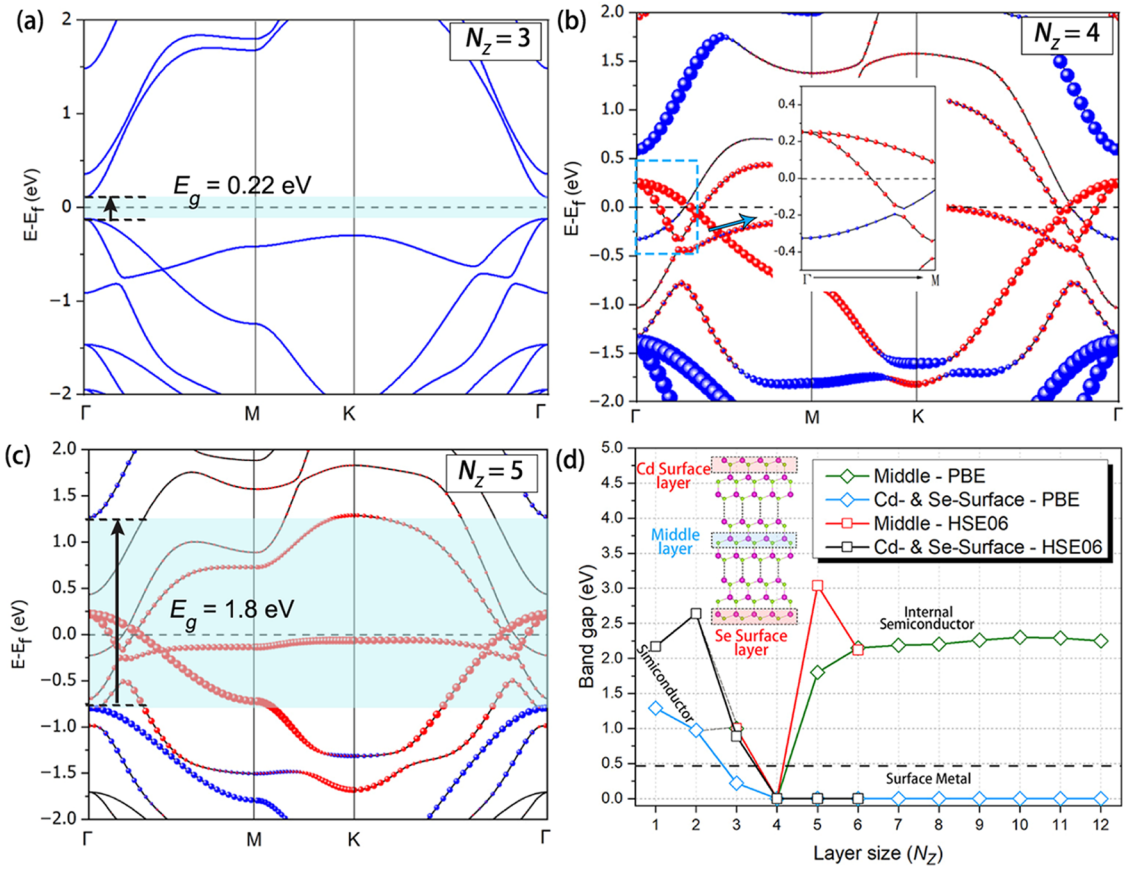

Figure 3. Layer-dependent band structure of the HC surface in the (111) slab model. Band structure of N_Z = (a) 3, (b) 4, and (c) 5. The red and blue spheres denote the bands contributed by the inside surface and internal region. (d) Band gap of the HC surface from N_Z = 1 to 12 by PBE and N_Z = 1−6 by HSE06 in the (111) slab. The green and red lines denote the inside semiconductive band gap. The blue and black lines denote the semiconductive band gap of the surface and the gapless metallic surface. The black dot line is the gap value (0.48 eV) in bulk CdSe.

these incomplete matched PDOS, especially the large charge intensity closing to the Fermi level (−0.5 eV), might make the (110) as-truncated surface configuration unstable. Therefore, the (110) slab should undergo spontaneous structure reconstruction to reduce the total energy of the system during the structural relaxation process. The Cd at the surface shows the inward movement to the inside layer, forming a Cd−Se plane, i.e., Cd is surrounded by three Se atoms. As shown in Figure 2c, the DOS peaks of the BTR surface shift to a lower energy level compared to the as-truncated structure, especially the peaks at −0.75 and −0.25 eV, and the peaks are particularly well aligned.

Size-Dependent Electronic Structures. It is known that the size effect of a nanostructure including nanoribbons, nanotubes, nanoholes, etc., significantly affects their physical properties. For example, the magnetic moment at the edge of 1T′-MoS_2 nanoribbon periodically variates depending on the odd and even widths.[53] In addition, the size effect will also induce the variation of the electronic structure of nanomaterials, such as the band gap of the graphene armchair nanoribbon sensitively depends on its width $N_Z = 3p - 1$, $3p$ or $3p + 1$ (where p is a positive integer number) when periodic holes are induced into it.[54] The stability and band gap of WZ CdSe based on the (0001) surface slabs oscillate with the number of odd and even layers.[39] Inspired by the above knowledge, we carefully investigated the size effect (the number of layers) related to the electronic structures of the CdSe (111) and (110) surface structures.

Layer-Dependent Semiconductor-to-Metallic Transition of (111) CdSe. The band structure of the (111) HC surface structure as the function of layer number N_Z from 1 to 12 was calculated as shown in Figure 3a−c (N_Z = 3, 4, and 5) and Figure S5 (other layers). It can be observed that CdSe shows direct semiconductivity when $N_Z < 4$. This is very similar to the bulk CdSe, i.e., both the CBM and VBM are located at Γ point. The band gap of the N_Z = 1, 2, and 3 (111) HC surface structure is ∼1.29, ∼0.95, and ∼0.22 eV, respectively. Furthermore, the projected band structure of N_Z = 4 is shown in Figure 3b. The red and blue balls denote the contribution from the surface and internal regions, respectively, while the layer number of each ball stands for the weight or probability. For N_Z = 4, both the surface and internal regions contribute to the VBM and CBM at Γ point, respectively. Compared to the band of N_Z = 3, the VBM from the surface region seems to shift upward and cross the Fermi level, while the CBM from the internal region shifts downward and crosses the Fermi level. The CdSe, therefore, unexpectedly transits to the metallic when N_Z increases to 4. For a larger layer number ($N_Z > 4$), the projected band of the surface and internal middle layers are in Figure 3c (N_Z = 5) and Figure S5c−i ($N_Z > 5$). It can be observed that the VBM from the surface layer also shifts higher to the Fermi level, showing the metallic character. However, the band structure from the internal middle layer acquires semiconductivity, as denoted by the blue ball in Figure 3c. It is still a direct semiconductor in which VBM and CBM are located at the Γ point with a ∼1.8 eV band gap. For

https://doi.org/10.1021/acsomega.4c06465
ACS Omega 2024, 9, 42488−42497

N_Z > 5, all of the CdSe shows the surface metallic and internal direct semiconductor characters as presented in Figure S5c−i. The band gap as a function of N_Z is summarized in Figure 3d. Obviously, the (111)-HC surface model of CdSe shows three different electronic properties as the change of layer number. When N_Z < 4, CdSe shows semiconductivity. When N_Z = 4, CdSe is completely metallic. When $N_Z \geq 5$, the surface region of CdSe shows a metallic character, while the internal region shows a semiconductor character. In addition, the hybrid functional (HSE06) calculation was also performed to calculate the band gap of (111)-HC surfaces from 1L to 6L. The band structures are shown in Figure S6, and the band gap is summarized in Figure 3d. The HSE06 results also show the semiconductor-to-surface metallic state transition as the layer size increases. Such results are similar to those of PBE.

To investigate the underlying mechanisms behind the sharp changes in the band gap related to N_Z, the charges of the Cd atom at the Cd-terminated surface and the Se atom at the Se-terminated surface of the (111)-HC slab (N_Z = 1 to 12) are summarized in Figure 4a. The negative charge of the Cd atom at the Cd surface increases gradually with the layer thickness. It is ~11.28e^- in the monolayer and reaches ~11.35e^- when N_Z increases to 6. The negative charge of the Se atom at the Se surface decreases gradually with an increase in N_Z. It is ~6.72 e^- when N_Z = 1 and reaches ~6.59e^- when N_Z increases to 6. Additionally, the z-direction electrostatic potential of the HC surface structure (N_Z = 1−5) is shown in Figure S7a. The bilayer system shows a balanced electrostatic potential in vacuum space. As the N_Z increases, the difference in the potential step at the vacuum space increases. The z-direction electrostatic potential in Figure S7a shows that polarization is present at the (111) surface with N_Z = 1, but electrons transfer from one side to another side should not take place. When N_Z = 2, the HC configuration shows a nonpolarized state (Figure S7b). Despite the polarization being observed in the N_Z = 3 system (Φ = 1.5), it is still not enough to cause a significant electron transfer and further make the CBM and VBM cross over at the Γ point because there is only ~0.6 eV potential increase from 1L to 3L. When N_Z increases to 4, the potential difference increases to ~2.5 eV (~1 eV increasing from 3L to 4L). The greatly enhanced potential difference should be derived from the increased polarization layer, as shown in Figure S7, leading to more electron transfer from the Se surface to the Cd surface. Ultimately, electron transfer from Se to Cd enables both the Cd and Se surfaces to be metallic. This suggests enhanced surface polarization with the increase in layer number. Therefore, more electrons are transferred from the Se surface to the Cd surface with an increase in the number of layers.

Figure 4b,4c depicts the projected bands of Cd and Se atoms at the bare Cd and Se surfaces of the HC surface when N_Z = 4, respectively. The CBM is mainly contributed by the electrons of surface Cd. It, thus, could be considered that more electrons are doped into surface Cd, causing an upward shift of the Fermi surface with the increase of N_Z. The CBM will move down and cross the Fermi surface, leading the Cd surface to become metallic and gain an electron pocket character at Γ after the so-called "electron doping" process, as depicted in Figure 4d. On the contrary, the electrons of Se at the Se surface contribute to the VBM. As the layer number increases, more electrons are transferred from the Se surface to the Cd surface. In other words, the positive hole could be regarded as doping at the Se-terminated surface. The Fermi surface,

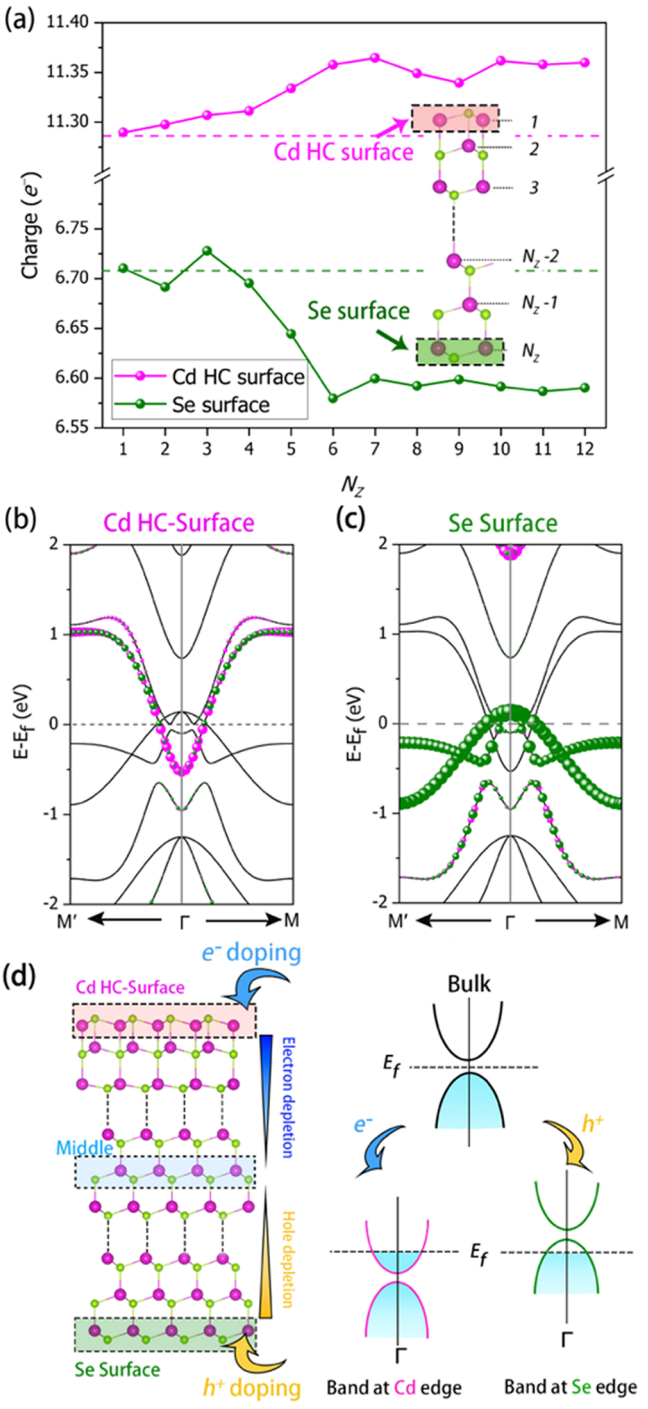

Figure 4. Analysis of metallic surface when N_Z > 3. (a) Negative charge of Cd and Se at the Cd-HC and Se surfaces, respectively. The projected bands of the N_Z = 4 HC surface along the (111) plane of (b) Cd at the HC surface and (c) Se at the Se surface. The red and green balls represent the band contributed by Cd and Se atoms, respectively. (d) Schematic figure of the charge transfer of the HC surface structure leading to the CBM and VBM shifts.

therefore, shifts downward to the lower energy level, and the VBM shifts upward, crossing the Fermi surface and then forming the hole pocket. This process leads the Se surface to become metallic. At the internal region (middle layers), the negative and positive charges keep neutral, i.e., close to the bulk state. That is why the internal region shows semiconductivity. The above process is schematically shown in

https://doi.org/10.1021/acsomega.4c06465
ACS Omega 2024, 9, 42488−42497

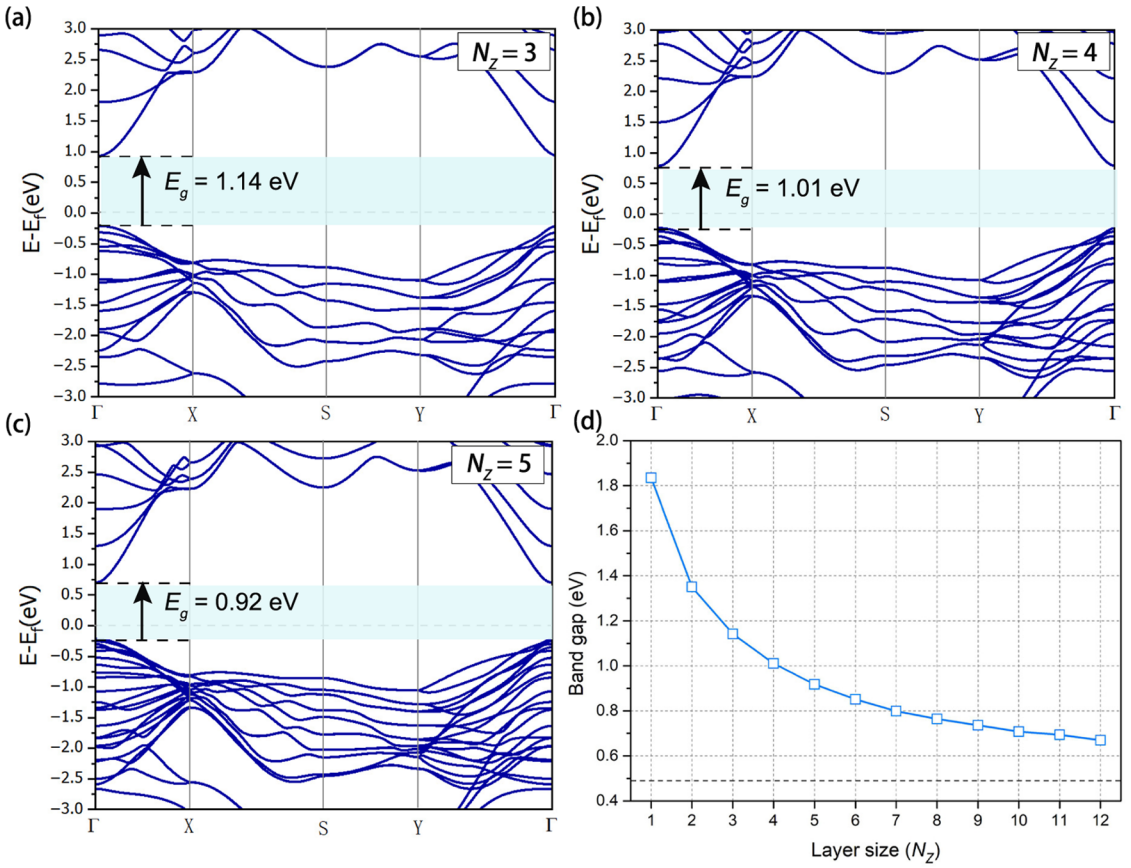

Figure 5. Layer-dependent band structure of the BTR surface in the (110) slab model. Band structure of N_Z = (a) 3, (b) 4, and (c) 5. (d) Band gaps as a function of the number of layers from N_Z = 1−12 in the (110) slab model. The black dot line is the gap value (∼0.48 eV) in bulk CdSe.

Figure 4d to illustrate the mechanism of the band structures of the (111)-HC surface depending on the layer number.

Layer-Dependent Band Structure of (110) CdSe. Figure 5 shows the layer-number-dependent (N_Z = 1−12) (110) BTR surface band structures. N_Z = 3, 4, and 5 are shown in Figure 5a−c, while the others are shown in Figure S8. All layers of CdSe show direct semiconductivity with both the CBM and VBM located at Γ. The band gap of N_Z = 1 and 2 is ∼1.83 and ∼1.35 eV, respectively, and the band gap of N_Z = 3 and 5 is ∼1.14 and ∼0.92 eV, respectively. The band gap as the function of N_Z is summarized in Figure 5d. It can be seen that the (110) BTR surface consistently maintains the same direct band gap semiconductor character as the bulk CdSe, and the band gap gradually decreases with the number of layers to close to that of the bulk CdSe. The *z*-direction electrostatic potential of the BTR surface structure (N_Z = 2, 3, and 5) is shown in Figure S7c. The potential shows a balance of electrostatic potential in the vacuum space regardless of N_Z. This indicates that there is no charge transfer among different layers, according to the Bader analysis in Table 1. Therefore, the (110) surface always remains semiconductive.

CONCLUSIONS

In this work, using DFT calculations, we investigated the surface reconstruction of CdSe and layer-number-dependent electronic properties. The HC configuration, ignored by previous studies, is energy-preferred compared with both the as-truncated and BTR configurations. In addition, it shows the semiconductor-to-metallic transition as the layer increases. When N_Z < 4, CdSe shows semiconductivity. When N_Z = 4, CdSe is completely metallic. When $N_Z \geq 5$, the surface region of CdSe remains metallic, while the internal region transits to semiconductivity. This metallic state surface derives from the intrinsic polarization of (111)-ZB CdSe. In contrast, the electronic properties of the (110) surface structure are independent of the layer number and only refer to the decrease in the band gap. In other words, it always remains a semiconductor. It should be attributed to the symmetrical structure at two side surfaces without charge transfer among different layers. Although experimental data of our findings on CdSe are still lacking, similar structures and properties have been observed experimentally in other materials, suggesting that our conclusions may be reasonable. For example, the HC configurations could be observed in GaX compounds.[45] In addition, Qin et al. also reported the successful growth of AlSb with a honeycomb surface structure on graphene-covered SiC (0001).[55] This also suggested the possibility of the HC configuration in (111) CdSe. Our finding not only revealed the additional possible surface structure but also clarified the underlying mechanism of metallic-to-semiconductor (even the edge metallic) transition related to the number of layers. Furthermore, ZB CdSe is characterized by its "layered" structure, consisting of six-membered rings with alternating Cd and Se atoms, with adjacent layers connected by covalent bonds. As a result, the stacking structures of the (111) and (110) surfaces are also representative, showing the typical zigzag and armchair characters, respectively. These surface configurations broadly exist in many other III−V, II−VI, and I−VII 2D materials, such as SiC, InSb, InAs, GaSb, GaAs, and HgTe.[43−45,56] Consequently, the insights and findings

https://doi.org/10.1021/acsomega.4c06465
ACS Omega 2024, 9, 42488−42497

presented in this work may inspire further study of surface configuration and electronic structures of other III−V, II−VI, and I−VII group MX compounds.

COMPUTATIONAL METHODS

Our DFT calculations were conducted by using the Vienna Ab inito Simulation Package (VASP).[57] The Perdew−Burke−Ernzerhof (PBE) exchange-correlation functional[58] and projector augmented wave method[59] were adopted. The Monkhorst−Pack k-point mesh of 3 × 3 × 3 was adopted for the first Brillouin zone in the calculations of the total energy and density of states (DOS) for bulk CdSe, and the tetrahedron method with Blöchl corrections was employed.[60] The Monkhorst−Pack k-point mesh was set as 7 × 7 × 1 for these as-truncated, BRT, and HC surfaces in the (111) surface from 1L to 12L to ensure that k-point sampling spacing is less than 0.2 $Å^{-1}$. The Monkhorst−Pack k-point mesh of 3 × 5 × 1 was set for the as-truncated and BTR surface along the (110) plane from 1L to 12L. Then, the atomic positions and lattice constants were fully relaxed until the total energy difference and forces were less than 10^{-5} eV and 0.01 eV/Å, respectively, with an energy cutoff of 500 eV for the plane-wave expansion. After full structure optimization, the BTR configuration of the (111) and (110) surfaces can be obtained. To construct the (111)-HC configuration, the Cd atoms on the surface layers are manually moved to the top of the Se atoms in the lower layer, and then the structure optimization was conducted with a similar convergence criterion in the previous. To avoid the metastable or saddle point state, the atomic position and lattice distortion were introduced. After full relaxation, the same structure was obtained, confirming its stability. Similar operations were also applied to the Se surface. A higher convergence criterion for total energy, 10^{-6} eV, was adopted to perform self-consistent calculations to obtain the electronic structures. Periodic boundary condition was applied in all three directions, and a 20 Å vacuum space was applied along the *z*-direction to avoid the interaction between two periodic images for all calculations.

ASSOCIATED CONTENT

Supporting Information

The Supporting Information is available free of charge at https://pubs.acs.org/doi/10.1021/acsomega.4c06465.

The energy of the (111) surface structures, the band structure of bulk CdSe, structures of the (111) and (110) surface model, the layer-dependent band structures of the (111) and (110) slab models, the *z*-direction electrostatic potential of the (111) and (110) surfaces, and all supplemental figures (PDF)

AUTHOR INFORMATION

Corresponding Authors

Kaiyun Chen − *Northwest Institute for Nonferrous Metal Research, Xi'an 710016, China;* orcid.org/0000-0003-1974-9428; Email: chenkaiyun309@gmail.com

Wangtu Huo − *Northwest Institute for Nonferrous Metal Research, Xi'an 710016, China*; Email: huowt@c-nin.com

Authors

Yuexin Dong − *School of Material Science and Engineering, Northeastern University, Shenyang 110819, China;*

Songrui Wei − *College of Physics and Optoelectronic Engineering, State Key Laboratory of Radio Frequency Heterogeneous Integration, Shenzhen University, Shenzhen 518060, China*

Le Zhang − *MOE Key Laboratory for Nonequilibrium Synthesis and Modulation of Condensed Matter, School of Physics, Xi'an Jiaotong University, Xian 710049, China;* orcid.org/0000-0003-4522-1555

Haoxi Dong − *MOE Key Laboratory for Nonequilibrium Synthesis and Modulation of Condensed Matter, School of Physics, Xi'an Jiaotong University, Xian 710049, China*

Cunle Bo − *MOE Key Laboratory for Nonequilibrium Synthesis and Modulation of Condensed Matter, School of Physics, Xi'an Jiaotong University, Xian 710049, China*

Complete contact information is available at: https://pubs.acs.org/10.1021/acsomega.4c06465

Notes

The authors declare no competing financial interest.

ACKNOWLEDGMENTS

The authors gratefully acknowledge the support of the National Natural Science Foundation of China (Grant Nos. 12204383, 22303068, 52102146, and 62105221), the Key Research and Development Projects of Shaanxi Province (Nos. 2024GX-YBXM-351 and 2024GX-YBXM-356), the Natural Science Basic Research Program of Shaanxi Province (2023-JC-QN-0123), the Research Startup Fund of the Northwest Institute for Nonferrous Metal Research (1201YK2408 and 1201YK2414). K.C. acknowledges the support from the Young Elite Scientists Sponsorship Program by CAST(2023QNRC001) and the Young Talent Fund of the Association for Science and Technology in Shaanxi (CLGC202201).

REFERENCES

(1) Zhao, X.; Song, K.; Huang, H.; Han, W.; Yang, Y. Ferroelectric Materials for Solar Energy Scavenging and Photodetectors. *Adv. Opt. Mater.* **2022**, *10*, No. 2101741.

(2) Omprakash, P.; Viswesh, P.; Devadas, B. P. Review-A Review of 2D Perovskites and Carbon-Based Nanomaterials for Applications in Solar Cells and Photodetectors. *ECS J. Solid State Sci. Technol.* **2021**, *10*, No. 031009.

(3) Wang, M.; Wang, W.; Ma, B.; Shen, W.; Liu, L.; Cao, K.; Chen, S.; Huang, W. Lead-Free Perovskite Materials for Solar Cells. *Nano−Micro Lett.* **2021**, *13*, 62.

(4) Zhang, J.; Feng, X.; Mei, L.; Yu, W.; Song, H.; Cui, N.; Yun, T.; Mu, H.; Lin, S. A $MAPbBr_3/PdSe_2$ Schottky junction-based optoelectronic sensor with self-powered and switchable photocurrents. *Mater. Des.* **2023**, *234*, No. 112368.

(5) Koppens, F. H. L.; Mueller, T.; Avouris, P.; Ferrari, A. C.; Vitiello, M. S.; Polini, M. Photodetectors based on graphene, other two-dimensional materials and hybrid systems. *Nat. Nanotechnol.* **2014**, *9*, 780−793.

(6) Liu, N.; Tian, H.; Schwartz, G.; Tok, J. B. H.; Ren, T.; Bao, Z. Large-Area, Transparent, and Flexible Infrared Photodetector Fabricated Using P-N Junctions Formed by N-Doping Chemical Vapor Deposition Grown Graphene. *Nano Lett.* **2014**, *14*, 3702−3708.

(7) Zhang, Y.; Vafaie, M.; Xu, J.; Pina, J. M.; Xia, P.; Najarian, A. M.; Atan, O.; Imran, M.; Xie, K.; Hoogland, S.; Sargent, E. H. Electron-Transport Layers Employing Strongly Bound Ligands Enhance

Stability in Colloidal Quantum Dot Infrared Photodetectors. *Adv. Mater.* **2022**, *34*, No. 2206884.
(8) Guo, R.; Zhang, M.; Ding, J.; Liu, A.; Huang, F.; Sheng, M. Advances in colloidal quantum dot-based photodetectors. *J. Mater. Chem. C* **2022**, *10*, 7404−7422.
(9) Wei, X.; Li, S.; Wang, W.; Zhang, X.; Zhou, W.; Xie, S.; Liu, H. Recent Advances in Structure Separation of Single-Wall Carbon Nanotubes and Their Application in Optics, Electronics, and Optoelectronics. *Adv. Sci.* **2022**, *9*, No. 2200054.
(10) Zhao, M.; Hao, Y.; Zhang, C.; Zhai, R.; Liu, B.; Liu, W.; Wang, C.; Jafri, S. H. M.; Razaq, A.; Papadakis, R.; Liu, J.; Ye, X.; Zheng, X.; Li, H. Advances in Two-Dimensional Materials for Optoelectronics Applications. *Crystals* **2022**, *12*, 1087.
(11) Gong, C.; Hu, K.; Wang, X.; Wangyang, P.; Yan, C.; Chu, J.; Liao, M.; Dai, L.; Zhai, T.; Wang, C.; Li, L.; Xiong, J. 2D Nanomaterial Arrays for Electronics and Optoelectronics. *Adv. Funct. Mater.* **2018**, *28*, No. 1706559.
(12) Novoselov, K. S.; Geim, A. K.; Morozov, S. V.; Jiang, D.; Zhang, Y.; Dubonos, S. V.; Grigorieva, I. V.; Firsov, A. A. Electric field effect in atomically thin carbon films. *Science* **2004**, *306*, 666−669.
(13) Wang, Q. H.; Kourosh, K. Z.; Kis, A.; Coleman, J. N.; Strano, M. S. Electronics and optoelectronics of two-dimensional transition metal dichalcogenides. *Nat. Nanotechnol.* **2012**, *7*, 699−712.
(14) Geim, A. K.; Grigorieva, I. V. Van der Waals heterostructures. *Nature* **2013**, *499*, 419−425.
(15) Novoselov, K. S.; Mishchenko, A.; Carvalho, A.; Castro Neto, A. H. 2D materials and van der Waals heterostructures. *Science* **2016**, *353*, No. eaac9439.
(16) Wang, Y.; Wang, L.; Zhang, X.; Liang, X.; Feng, Y.; Feng, W. Two-dimensional nanomaterials with engineered bandgap: Synthesis, properties, applications. *Nano Today* **2021**, *37*, No. 101059.
(17) Xu, M.; Liang, T.; Shi, M.; Chen, H. Graphene-Like Two-Dimensional Materials. *Chem. Rev.* **2013**, *113*, 3766−3798.
(18) Shan, G.; Tan, H.; Ma, R.; Zhao, H.; Huang, W. Recent progress in emergent two-dimensional silicene. *Nanoscale* **2023**, *15*, 2982−2996.
(19) Choi, W.; Choudhary, N.; Han, G. H.; Park, J.; Akinwande, D.; Lee, Y. H. Recent development of two-dimensional transition metal dichalcogenides and their applications. *Mater. Today* **2017**, *20*, 116−130.
(20) Velusamy, D. B.; Kim, R. H.; Cha, S.; Huh, J.; Khazaeinezhad, R.; Kassani, S. H.; Song, G.; Cho, S. M.; Cho, S. H.; Hwang, I.; Lee, J.; Oh, K.; Choi, H.; Park, C. Flexible transition metal dichalcogenide nanosheets for band-selective photodetection. *Nat. Commun.* **2015**, *6*, No. 8063.
(21) Elbanna, A.; Jiang, H.; Fu, Q.; Zhu, J.; Liu, Y.; Zhao, M.; Liu, D.; Lai, S.; Chua, X.; Pan, J.; Shen, Z.; Wu, L.; Liu, Z.; Qiu, C.; Teng, J. 2D Material Infrared Photonics and Plasmonics. *ACS Nano* **2023**, *17*, 4134−4179.
(22) Malik, M.; Iqbal, M. A.; Choi, J. R.; Pham, P. V. 2D Materials for Efficient Photodetection: Overview, Mechanisms, Performance and UV-IR Range Applications. *Front. Chem.* **2022**, *10*, No. 905404.
(23) Wang, G.; Zhang, Y.; You, C.; Liu, B.; Yang, Y.; Li, H.; Cui, A.; Liu, D.; Yan, H. Two dimensional materials based photodetectors. *Infrared Phys. Technol.* **2018**, *88*, 149−173.
(24) Li, Z.; Yan, H.; Liu, X.; Liu, S.; Feng, M.; Wang, X.; Yan, B.; Xue, D. Surface-Defect States in Photovoltaic Absorber GeSe. *J. Phys. Chem. Lett.* **2021**, *12*, 10249−10254.
(25) Sawada, K.; Iwata, J. I.; Oshiyama, A. Spontaneous appearance of a low-dimensional magnetic electron system on semiconductor nanostructures. *Phys. Rev. B* **2016**, *93*, No. 235421.
(26) Liu, H.; Gong, H.; Liu, K.; Ding, K.; Chen, J.; Liu, Z.; Rao, F. Electronic Excitation-Induced Semiconductor-Metal Transitions Enabling Ovonic Threshold Switching in Boron Telluride Glasses. *Chem. Mater.* **2023**, *35*, 6396−6404.
(27) Lei, F.; Sun, Y.; Liu, K.; Gao, S.; Liang, L.; Pan, B.; Xie, Y. Oxygen Vacancies Confined in Ultrathin Indium Oxide Porous Sheets for Promoted Visible-Light Water Splitting. *J. Am. Chem. Soc.* **2014**, *136*, 6826−6829.
(28) Zheng, P.; Jiang, Y.; Li, H.; Dai, X. Electron transport properties of $PtSe_2$ nanoribbons with distinct edge reconstructions. *RSC Adv.* **2022**, *12*, 25872−25880.
(29) Deng, X.; Li, Z.; Yang, J. One-Dimensional Magnetic Order Stabilized in Edge-Reconstructed MoS_2 Nanoribbon via Bias Voltage. *J. Phys. Chem. Lett.* **2020**, *11*, 7531−7535.
(30) Smith, A. M.; Mohs, A. M.; Nie, S. Tuning the optical and electronic properties of colloidal nanocrystals by lattice strain. *Nat. Nanotechnol.* **2009**, *4*, 56−63.
(31) Justo, Y.; Goris, B.; Kamal, J. S.; Geiregat, P.; Bals, S.; Hens, Z. Multiple Dot-in-Rod PbS/CdS Heterostructures with High Photoluminescence Quantum Yield in the Near-Infrared. *J. Am. Chem. Soc.* **2012**, *134*, 5484−5487.
(32) Ithurria, S.; Bousquet, G.; Dubertret, B. Continuous Transition from 3D to 1D Confinement Observed during the Formation of CdSe Nanoplatelets. *J. Am. Chem. Soc.* **2011**, *133*, 3070−3077.
(33) Li, Q.; Lian, T. Exciton Spatial Coherence and Optical Gain in Colloidal Two-Dimensional Cadmium Chalcogenide Nanoplatelets. *Acc. Chem. Res.* **2019**, *52*, 2684−2693.
(34) Peng, Z. A.; Peng, X. Formation of high-quality CdTe, CdSe, and CdS nanocrystals using CdO as precursor. *J. Am. Chem. Soc.* **2001**, *123*, 183−184.
(35) Alivisatos, A. P. Semiconductor clusters, nanocrystals, and quantum dots. *Science* **1996**, *271*, 933−937.
(36) Liu, Y. H.; Wang, F.; Wang, Y.; Gibbons, P. C.; Buhro, W. E. Lamellar Assembly of Cadmium Selenide Nanoclusters into Quantum Belts. *J. Am. Chem. Soc.* **2011**, *133*, 17005−17013.
(37) Thoma, S. G.; Sanchez, A.; Provencio, P. P.; Abrams, B. L.; Wilcoxon, J. P. Synthesis, optical properties, and growth mechanism of blue-emitting CdSe nanorods. *J. Am. Chem. Soc.* **2005**, *127*, 7611−7614.
(38) Joo, J.; Jae, S.; Koon, G.; Jung, H.; Hwanhyeon, T. Low-temperature solution-phase synthesis of quantum well structured CdSe nanoribbons. *J. Am. Chem. Soc.* **2006**, *128*, 5632−5633.
(39) Devi, P.; Mahendiran, D.; Murugan, P. First principles study on thickness dependent structural and electronic properties unveiling the growth and stability of 2D layered II-VI semiconducting compounds. *Phys. Chem. Chem. Phys.* **2022**, *24*, 24296−24305.
(40) Datta, S.; Dasgupta, T. S.; Sarma, D. D. Wannier function study of the relative stability of zinc-blende and wurtzite structures in the CdX (X = S, Se, Te) series. *J. Phys.: Condens. Matter* **2008**, *20*, No. 445217.
(41) Tong, C.-J.; Zhang, H.; Zhang, Y.; Liu, H.; Liu, L. New manifold two-dimensional single-layer structures of zinc-blende compounds. *J. Mater. Chem. A* **2014**, *2*, 17971−17978.
(42) Cui, X. Y.; Delley, B.; Stampfl, C. Band gap engineering of wurtzite and zinc-blende GaN/AlN superlattices from first principles. *J. Appl. Phys.* **2010**, *108*, No. 103701, DOI: 10.1063/1.3505752.
(43) Zhou, J.; Huang, J.; Sumpter, B. G.; Kent, P. R. C.; Terrones, H.; Smith, S. C. Structures, Energetics, and Electronic Properties of Layered Materials and Nanotubes of Cadmium Chalcogenides. *J. Phys. Chem. C* **2013**, *117*, 25817−25825.
(44) Zhou, J.; Huang, J.; Sumpter, B. G.; Kent, P. R. C.; Xie, Y.; Terrones, H.; Smith, S. C. Theoretical Predictions of Freestanding Honeycomb Sheets of Cadmium Chalcogenides. *J. Phys. Chem. C* **2014**, *118*, 16236−16245.
(45) Lucking, M. C.; Xie, W.; Choe, D. H.; West, D.; Lu, T. M.; Zhang, S. B. Traditional Semiconductors in the Two-Dimensional Limit. *Phys. Rev. Lett.* **2018**, *120*, No. 086101.
(46) Zhou, Z.; Li, J.; Fan, Y.; Zhang, Q.; Lu, X.; Fan, S.; Kikuchi, K.; Nomura, N.; Kawasaki, A.; Wang, L.; Jiang, W. Uniform dispersion of SiC in Yb-filled skutterudite nanocomposites with high thermoelectric and mechanical performance. *Scr. Mater.* **2019**, *162*, 166−171.
(47) Catti, M. Orthorhombic intermediate state in the zinc blende to rocksalt transformation path of SiC at high pressure. *Phys. Rev. Lett.* **2001**, *87*, No. 035504.
(48) Ouendadji, S.; Ghemid, S.; Meradji, H.; Hassan, F. E. H. Theoretical study of structural, electronic, and thermal properties of

https://doi.org/10.1021/acsomega.4c06465
ACS Omega 2024, 9, 42488−42497

CdS, CdSe and CdTe compounds. *Comput. Mater. Sci.* **2011**, *50*, 1460−1466.
(49) Deligoz, E.; Colakoglu, K.; Ciftci, Y. Elastic, electronic, and lattice dynamical properties of CdS, CdSe, and CdTe. *Physica B* **2006**, *373*, 124−130.
(50) Bai, S.; Devaty, R. P.; Choyke, W. J.; Kaiser, U.; Wagner, G.; MacMillan, M. F. Determination of the electric field in 4H/3C/4H-SiC quantum wells due to spontaneous polarization in the 4H SiC matrix. *Appl. Phys. Lett.* **2003**, *83*, 3171−3173.
(51) Polyakov, V. M.; Schwierz, F. Formation of two-dimensional electron gases in polytypic SiC heterostructures. *J. Appl. Phys.* **2005**, *98*, No. 023709.
(52) Akiyama, T.; Kawamura, T.; Ito, T. Computational discovery of stable phases of graphene and h-BN van der Waals heterostructures composed of group III-V binary compounds. *Appl. Phys. Lett.* **2021**, *118*, No. 023101.
(53) Chen, K.; Deng, J.; Ding, X.; Sun, J.; Yang, S.; Liu, J. Z. Ferromagnetism of 1T′-MoS_2 Nanoribbons Stabilized by Edge Reconstruction and Its Periodic Variation on Nanoribbons Width. *J. Am. Chem. Soc.* **2018**, *140*, 16206−16212.
(54) Tian, W.; Zeng, Y.; Zhang, Z. Electronic properties of graphene nanoribbons with periodically hexagonal nanoholes. *J. Appl. Phys.* **2013**, *114*, No. 074307.
(55) Qin, L.; Zhang, Z. H.; Jiang, Z. Y.; Fan, K.; Zhang, W. H.; Tang, Q. Y.; Xia, H. N.; Meng, F. Q.; Zhang, Q. H.; Gu, L.; West, D.; Zhang, S. B.; Fu, Y. S. Realization of AISb in the Double-Layer Honeycomb Structure: A Robust Class of Two-Dimensional Material. *ACS Nano* **2021**, *15*, 8184−8191.
(56) Zhang, J.-M.; Zheng, F.; Zhang, Y.; Ji, V. First-principles study on electronic properties of SiC nanoribbon. *J. Mater. Sci.* **2010**, *45*, 3259−3265.
(57) Kresse, J. G.; Furthmüller, J. Efficiency of ab-initio total energy calculations for metals and semiconductors using a plane-wave basis set. *Comput. Mater. Sci.* **1996**, *6*, 15−50.
(58) Perdew, J. P.; Chevary, J.; Vosko, S.; Jackson, K.; Pederson, M.; Singh, D.; Fiolhais, C. Atoms; molecules solids and surfaces: Applications of the generalized gradient approximation for exchange and correlation. *Phys. Rev. B* **1992**, *46*, 6671−6687.
(59) Blöchl, P. E. Projector augmented-wave method. *Phys. Rev. B* **1994**, *50*, 17953−17979.
(60) Blöchl, P. E.; Jepsen, O.; Andersen, O. K. Improved tetrahedron method for Brillouin-zone integrations. *Phys. Rev. B* **1994**, *49*, No. 094515.

https://doi.org/10.1021/acsomega.4c06465
ACS Omega 2024, 9, 42488−42497